analytical chemistry

pubs.acs.org/ac Article

# Ternary Z-Scheme Ag-Embedded $TiO_2$–$Ag_2S$ Nanojunction as a Novel Photoelectrochemical Converter for CD44 Detection

Yue Jia,† Rui Xu,† Kun Xu, Shoufeng Wang, Xiang Ren, Nuo Zhang, Dan Wu, Hongmin Ma, Yuyang Li,* and Qin Wei*

Cite This: *Anal. Chem.* 2022, 94, 11713–11720 Read Online

ACCESS | Metrics & More | Article Recommendations | Supporting Information

**ABSTRACT:** Nanoarrays (NAs) with stable signal output have become the most promising photoelectrochemical (PEC) biosensing substrate. However, a general issue is that interfacial charge-carrier recombination in a single-component semiconductor cannot be easily prevented, resulting in a low photocurrent density. Herein, a biosensor utilizing a Ag-embedded $TiO_2$–$Ag_2S$ nanojunction ($TiO_2$–Ag–$Ag_2S$) as a signal converter was developed for the detection of CD44 protein—a transmembrane glycoprotein highly expressed in breast cancer cells. The ternary Z-scheme heterojunction was prepared by a distinctive scheme in which the Ag layer is introduced onto the surface of rutile $TiO_2$ NAs by magnetron sputtering, whereas the $Ag_2S$ is rooted in the local sulfuration of Ag. With a sufficient density of oriented nanorods, $TiO_2$–Ag–$Ag_2S$ exhibits a smooth photocurrent output and minimal variation among different batches; it is undoubtedly a satisfactory PEC sensing carrier, which enables highly specific identification of target CD44 on the surface of MDA-MB-231 cells due to DNA strand displacement reactions (SDRs) and host–guest recognition between hyaluronic acid (HA) and CD44. The biosensor shows a sensitive PEC response to CD44 over a wide range of 37 to $5.0 \times 10^5$ cells/mL. We can conclude that this approach will provide an alternative solution to breast cancer diagnosis.

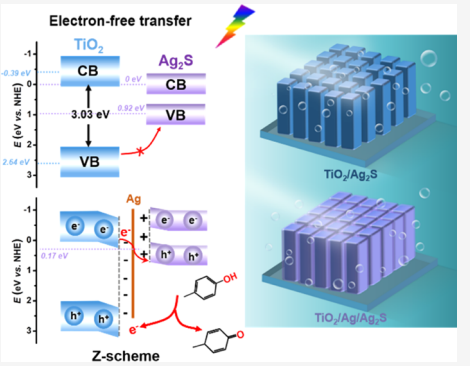




"Pink slayer"—breast cancer—has replaced lung cancer as the world's leading cancer since 2020. However, the gospel is that the survival rate of early breast cancer after surgery ranges from 95 to 97% within 5 years, which illustrates that the early diagnosis of breast cancer can effectively reduce mortality. CD44 is a transmembrane glycoprotein on the cell surface that is highly expressed in breast cancer cells, participates in heterogeneous adhesion, and plays a promoting role in the invasion and metastasis of cancer cells. Photoelectrochemical (PEC) biosensors are signal converters that can be used to convert the target concentration to a visible photocurrent density and have been widely used in the detection of antigens, nucleic acids, metal ions, and lipid carbohydrates.[1−3] In recent years, researchers have focused on how to improve the stability of sensors, including the signal output stability of a single sensor and narrowing the differences between production batches of sensors. Nanoarrays (NAs) are widely recognized as satisfactory sensing substrates because their exposed active regions are effective for PEC emission due to the improved electron transport along the ordered one-dimensional (1D) or two-dimensional (2D) array structure.[4] However, a general issue is that interfacial charge-carrier recombination in single-component NAs cannot be easily overcome, resulting in a low photocurrent density.[5] Although the construction of heterojunctions can ameliorate this problem, it is difficult to prepare nanocomposite arrays that can retain the as-prepared micromorphology due to the growth principle of different crystal structures.

The discovery of titanium dioxide ($TiO_2$) is one of the greatest revolutions in the world of materials science. We have no reasons to doubt its outstanding contribution in the fields of industry, food, the environment, and cosmetics due to its irreplaceable and excellent properties.[6] Current research mainly focuses on the expansion of its potential in PEC catalysis and sensing. However, material modification is essential because the wide band gap of $TiO_2$ entails the use of a high-energy light source for the photogeneration of electron–hole pairs ($e^-/h^+$).[7] Compared with material modification methods based on ion doping, dye, or quantum dot sensitization, heterostructure fabrication yields more satisfactory results than other deficient methods; for instance, the impurity level formed by ion doping can form recombination centers for electrons and holes, while deposition of noble metals emphasizes more fiscal expenditure and instability in catalytic reactions.[8−12] In 2006, Tada et al.

**Received:** July 14, 2022
**Accepted:** August 5, 2022
**Published:** August 12, 2022

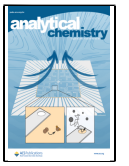




https://doi.org/10.1021/acs.analchem.2c03046
*Anal. Chem.* 2022, 94, 11713–11720

proposed an all-solid-state Z-scheme nanojunction utilizing a gold layer as an electron intermediary as a result of vectorial electron transfer driven by two-step excitation between $TiO_2$ and CdS.[13] A novel idea is provided by merging the character of Schottky junctions and surface plasmons in semiconductor−metal heterojunctions. Many similar ternary nanojunctions, for instance, $TiO_2$/Ag−$Ag_2S$, CdS−Ag−$TiO_2$, $TiO_2$/$WO_3$/Pt, and $g$-$C_3N_4$/Pd/$TiO_2$, have been proposed, and they all use the same preparation scheme, in which the introduction of a noble-metal layer depends on the reduction of the salt solution.[14−17] This is undoubtedly satisfactory for photocatalysis, but we think this may not be a good enough scheme for biosensing, which requires strict photocurrent stability.

A Z-scheme heterojunction, a special nanojunction similar to type-II in the matching band gap, is formed at the microscopic interface between two semiconductor phases with stepped energy bands.[18] In a Z-scheme nanojunction, the electrons flow to the conduction band (CB) with stronger reducing power while the holes accumulate in the valence band (VB), which has greater oxidation capacity.[19] This structure will give the nanocomposites stronger redox characteristics, it cannot be achieved in type-I and type-II nanojunctions.[20] It is not easy to design a heterojunction to meet our expectations. This requires a coincidental energy band for matching the other semiconductor phase with $TiO_2$ and a mass of convincing evidence. Another tricky question is how to identify the Z-scheme, type-I, and type-II structures. The most common method is to consider the redox potential of both whose range is wider is the Z-scheme.[21,22] This poses the redox potential of the reactants to be between the energy bands of two semiconductors, and the heterojunction type depends on whether there is any product formation. These are both a judgment condition and limitation because they may not exist at the same time.

In this work, we successfully prepared a ternary Z-scheme $TiO_2$−Ag−$Ag_2S$ nanojunction via three procedures. Rutile $TiO_2$ nanoarrays (NAs) are first grown on a fluorine-doped stannic oxide (FTO) electrode by a hydrothermal reaction. The noble-metal elementary substance-state silver (Ag) layer is introduced to the surface of $TiO_2$ by means of magnetron sputtering, whereas $Ag_2S$ is rooted in the local sulfuration of the Ag layer. The morphologically stable ternary nanojunction is confirmed to be a Z-scheme by electron paramagnetic resonance (EPR), in situ irradiation X-ray photoelectron spectroscopy (ISI-XPS), and high-angle annular dark-field scanning transmission electron microscopy (HAADF-STEM). This is a promising path to synthesize well-ordered ternary or even binary heterojunctions for adjusting the energy band structure of photoactive electrodes or photocatalysts. Meanwhile, a DNA strand displacement reaction (SDR) was introduced to extract CD44 from the surface of MDA-MB-231 breast cancer cells by the double action of endonuclide shearing and hyaluronic acid (HA) host−guest recognition of CD44.[23,24] With stable signal outputs and minimal variation in biosensor batches, the as-prepared sensing platform is found to show an excellent PEC response to CD44.

## EXPERIMENTAL SECTION

**Chemicals.** All reagents were commercially available and used without further purification: tetrabutyl titanate ($C_{16}H_{36}O_4Ti$, AR), 6-mercapto-1-hexanol (MCH, 98%), sodium sulfide ($Na_2S$, 90%), and tyrosine (Y, 98%) were purchased from Shanghai Macklin Biochemical Co., Ltd. Fetal calf serum (FBS, GR) and trypsin-ethylene diamine tetraacetic acid (trypsin-EDTA, GR) were purchased from Thermo Fisher Scientific, Inc. Hyaluronic acid (HA, 5 kDa) was purchased from Lifecore Biomedical, Inc. 1 × phosphate-buffered saline (PBS) (pH 7.2−7.4) was obtained from Beijing Solarbio Technology Co., Ltd. 1 × Tris−EDTA (TE) buffer and oligonucleotides were synthesized by Shanghai Sangon Biological Engineering Technology and Services Co., Ltd., and their sequences (5′ → 3′) are expressed as follows: H1 SH-TAC TAT AAA GTG TAA GTA GTC TAG ACG TAG CTG ATT TTA TTA CAC GCC GAA TCC TAG ACT ACTT; P1 AAC CTC AGC TAC GTC TAG ACT ACT TAC ACTT-$NH_2$; P2 TCT AGA CGT AGC TGA GGTT-$NH_2$. Deionized (DI) water with an electrical resistance of 18.25 MΩ/cm was used throughout the experiments.

**Characterization.** Magnetron sputtering was carried out using a VJC-400 magnetron sputtering system (Vnano, China). Ion beam sputtering was completed using an Agar Scientific coating machine (Oxford, U.K.). The crystal structure and phase composition of the samples were studied by a D8 Focus X-ray diffraction (XRD) system (Bruker, Germany) and a TalosF200x high-resolution transmission electron microscopy (HRTEM) imaging system (FEI). Ultraviolet−visible (UV−vis) absorption and diffuse-reflectance spectra (DRS) were obtained by using a UV-3600 Plus spectrophotometer (Shimadzu, Japan). The $^{\bullet}OH$ radical species test was carried out using an EMXnano electron paramagnetic resonance (EPR) spectrometer (Bruker, Germany). The morphology of the sample at different stages was observed via a Mira Lms field emission scanning electron microscope (FESEM) (Tescan, Czech Republic) and a TalosF200x high-angle annular dark-field scanning transmission electron microscopy (HAADF-STEM) imaging system (FEI), which was equipped with a Super-X energy dispersive spectrometer (EDS) for the evaluation of the elemental distribution. The elemental composition, valence, and electron cloud density were analyzed by a PHI-5000VersaprobeIII ISI-XPS spectrometer equipped with a xenon (Xe) lamp (ULVAC-PHI, Japan). The electrochemical tests were performed using a CHI760E electrochemical workstation (Chenhua, China).

**Preparation of Rutile $TiO_2$ NAs.** The $TiO_2$ NAs were grown onto an FTO electrode by a minor modification to a method that we have proposed earlier.[25] A mixture containing 8 mL of 12 M hydrochloric acid (HCl), 8 mL of DI water, and 0.2 mL of $C_{16}H_{36}O_4Ti$ was vigorously stirred and transferred to a 50 mL Teflon-lined stainless-steel autoclave. After a sheet of FTO (2 × 2 $cm^2$) with an upturned conductive surface was laid at the bottom of the reactor, the entire sheet was kept at 150 °C for 10 h to obtain the preliminary product. Successful synthesis entails the absence of solids anywhere except for a translucent film on the surface of FTO. Finally, the semifinished $TiO_2$ NAs were annealed at 500 °C for 2 h to enhance the crystallinity.

**Sputtering of the Ag Overlayer.** An Ag layer was deposited onto the surface of the $TiO_2$ NAs using magnetron sputtering at room temperature. The sputtering deposition was performed in an argon atmosphere at a total working pressure of 1.3 Pa, and the power was held constant at 60 W for 3 min to obtain the $TiO_2$−Ag composite.

**Sulfidation of the Ag Overlayer.** An in situ Ag overlayer sulfidation method was employed based on the process shown in eq 1.[26] The as-prepared $TiO_2$−Ag was immersed in 2 M $Na_2S$ aqueous solution for 12 h after bubbling with oxygen.


https://doi.org/10.1021/acs.analchem.2c03046
Anal. Chem. 2022, 94, 11713−11720

The obtained $TiO_2$−Ag−$Ag_2S$ electrode was repeatedly washed with DI water for further use.

$$4Ag + 2S^{2-} + O_2 + 2H_2O \rightarrow 2Ag_2S + 4OH^- \quad (1)$$

**Cell Culture and Collection.** MDA-MB-231 cells, a human breast cell line, were cultured in 10% (v/v) fetal bovine serum-filled Dulbecco's modified Eagle's medium (DMEM) and maintained at 37 °C in a humid atmosphere with 5% $CO_2$. Adherent MDA-MB-231 cells were digested with 0.25% trypsin-EDTA digestive juice. After centrifugal washing for 10 min at 1000 rpm using 1 × PBS, the obtained MDA-MB-231 cells were dispersed to different concentrations for further use.

**Extraction of CD44 from the Cell Surface.** HA (20 mg) was irradiated and sterilized by a UV lamp for 2 h and then dissolved into 20 mL of 1 × PBS. Single-stranded DNA P2 (ssDNA-P2, 1 mL, 1 mM) was mixed with 5 mL of the above HA solution activated by EDC (0.01 M) to form conjugate P2−HA. Another simultaneous amidation occurred between the carboxyl-activated tyrosine (Y, 1 mM) and ssDNA-P1 (1 mM), eventually forming the coupling (Y−P1). This leads to the local formation of base pairs to produce duplex DNA Y−P1−P2−HA. Then, 200 μL of Y−P1−P2−HA was added to each hole in a 24-well plate. Next, MDA-MB-231 cells with different concentrations were added to each well for host−guest recognition for 0.5 h. After centrifugation, the lower substrate was redispersed in the same amount of 1 × PBS and then 50 U Nt.BbvCI was added and kept at 37 °C for 2 h. The enzymolysis products were stored at 37 °C for further use.

**Fabrication of the Biosensor.** As shown in Scheme 1, the as-synthesized $TiO_2$−Ag−$Ag_2S$ was covered with a layer of gold nanoparticles by ion beam sputtering for 20 s with a stable 220 V alternating voltage and 10 mA current. The effective area of light is restricted by a nontransparent adhesive sticker using a circular hole with a diameter of 3 mm. Later, the 3′-terminus of the hairpin probe (H1) was modified with a sulfhydryl (−SH) and immobilized onto the $TiO_2$−Ag−$Ag_2S$ surface by immersing the electrode into H1 solution (1 mM). Then, 6 μL of MCH (5%) was used to block the gold active sites. Before drying, the electrode was immersed in the final solution of enzymolysis products for 12 h to complete the final strand replacement reaction. The sensor fabrication was completed after cleaning the electrode with PBS.

**Scheme 1. Schematic Diagrams Showing Fabrication of the PEC Biosensor**

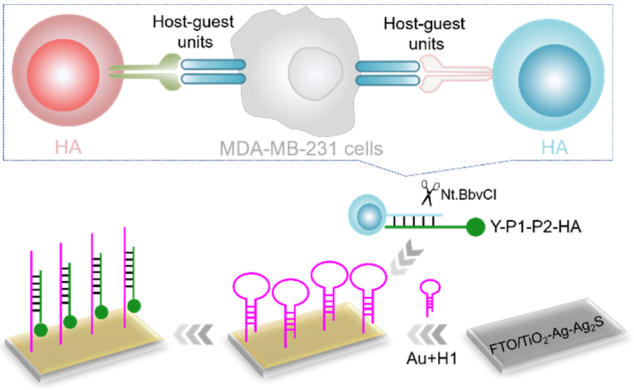


**PEC Measurements of CD44.** The PEC measurements were carried out utilizing a three-electrode system with Pt wire, Ag/AgCl, and the as-purposed biosensor as the counter electrode, reference electrode, and working electrode, respectively. A 0.1 M carbonate buffer solution (CBS, pH 9.8) was used as the electrolyte, and a Xe lamp was used as the illumination source with a power of 100 W.

## RESULTS AND DISCUSSION

**Characterization of $TiO_2$, $TiO_2$−Ag, and $TiO_2$−Ag−$Ag_2S$.** The crystal structures of the ternary $TiO_2$−Ag−$Ag_2S$ hybrids were analyzed by XRD, and the patterns are presented in Figure S1. $TiO_2$-covered FTO exhibits six characteristic peaks for $SnO_2$ with 2$\theta$ values equal to 26.58, 33.77, 37.77, 51.76, 61.75, and 65.74° (pattern i, PDF#46-1088). The diffraction peak for rutile $TiO_2$(101) is found at a 2$\theta$ value equal to 36.09°, and a small number of (211), (301), and (112) lattice planes are exposed at 2$\theta$ values of 54.32, 69.20, and 69.79° (PDF#21-1276). The target material for magnetron sputtering is face-centered cubic Ag (pattern ii). In pattern iii, the presence of Ag metal is also found, but five weak peaks are also found at 2$\theta$ values ranging from 28.97 to 34.70°, which correspond to monoclinic crystal $Ag_2S$ (PDF#14-0072). The results confirm that the sulfuration is local and that Ag metal exists in the cracks of the ternary system, which is what we expected.

HRTEM was employed to further characterize the crystal structure of $TiO_2$−Ag−$Ag_2S$. The rod-like major structure of $TiO_2$ and $Ag_2S$ crystals attached to its surface can be observed in Figure 1a, and a highly crystallized recombination state for $TiO_2$−Ag−$Ag_2S$ can be observed in Figure 1b. Two high-density lattice fringes are observed with lattice constants of 2.5 and 2.8 Å, which are attributed to the (101) plane of $TiO_2$ and (−112) plane of $Ag_2S$, respectively, with no obvious buffer zone between these planes. Local sulfuration of the Ag layer is the key to the preparation of the composites, and HAADF-STEM elemental mapping was carried out on the material to evaluate the atom distribution of the random region. Figure 1c provides us with a highly consistent distribution of Ti and O atoms, while regional differences exist between Ag and S atoms, which is important evidence for the existence of the Ag layer. The EDS spectrum (Figure 1d) offers specific atomic ratios, where the atomic fractions of Ti, O, Ag, and S are 31.60, 67.62, 0.42, and 0.36%, respectively.

FESEM was employed to observe the morphological changes in the material surface. Pure $TiO_2$ with uniform density nanorod arrays is observed in Figure 2a,b under plotting scales. It is clear that the cross profile of the nanorods resembles a broken structural orientation, which is an inevitable sign of one-dimensional growth. When the $TiO_2$ surface is covered by sputtered silver, the accumulation of silver particles enhances the conductivity of the interface, which can be verified by the change in contrast. More importantly, the silver nanoparticles from the nanorods gap into the firmly loaded $TiO_2$ surface, making its surface smooth compared with that before (Figure 2c,d). A major change in morphology occurs after in situ sulfidation. As shown in Figure 2e,f, the endpoint of the nanorods is observed to undergo a similar change from melting to solidification, and a large amount of $Ag_2S$ endows the package with good conductivity and smoothness exposed to the interface. The elements show a balanced distribution (Figure S2). In this process, the microscopic order of $TiO_2$ is not destroyed, which is rare,


https://doi.org/10.1021/acs.analchem.2c03046
Anal. Chem. 2022, 94, 11713−11720

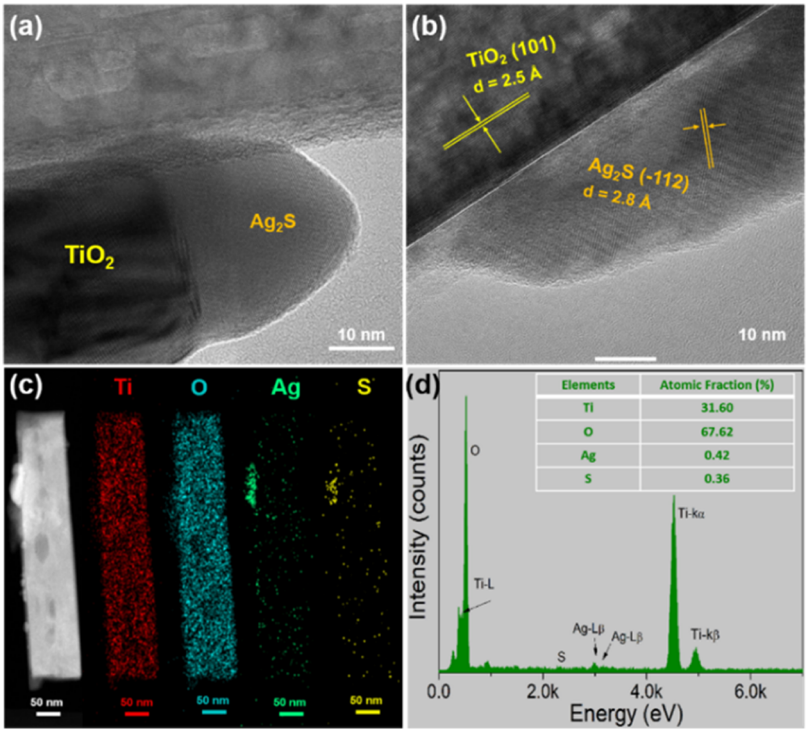


**Figure 1.** (a, b) HRTEM images of $TiO_2$−Ag−$Ag_2S$. (c) HAADF-STEM image of $TiO_2$−Ag−$Ag_2S$ and its corresponding elemental mapping images of Ti, O, Ag, and S. (d) EDS spectrum and atomic fraction determined from the STEM image.

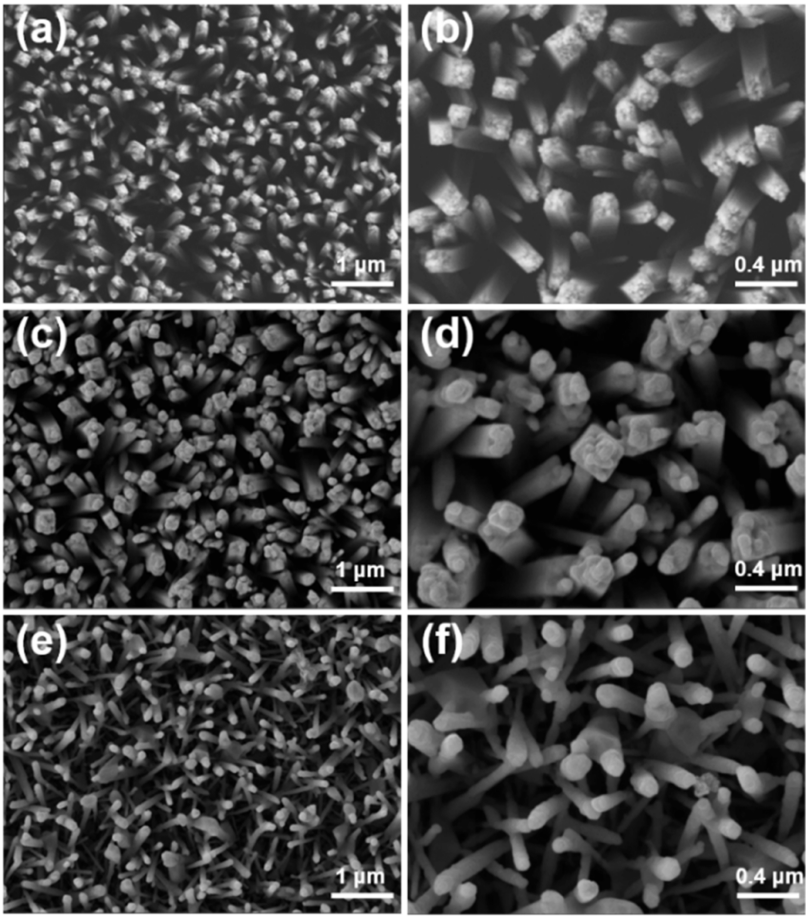


**Figure 2.** FESEM images of pure $TiO_2$ (a, b), $TiO_2$−Ag (c, d), and $TiO_2$−Ag−$Ag_2S$ (e, f).



https://doi.org/10.1021/acs.analchem.2c03046
Anal. Chem. 2022, 94, 11713−11720

and its microscopic morphology is in line with our expectations.

**Heterojunction Evaluation of $TiO_2$−Ag−$Ag_2S$.** Analysis of the band gap structure is the most important basis from which to judge the heterojunction type. The UV−vis absorption spectra are first provided in Figure S3a. $TiO_2$−Ag−$Ag_2S$ shows a wide visible light absorption range compared to pure $TiO_2$, which is a common feature of narrow-band-gap semiconductors. The energy gap of $TiO_2$ is calculated to be approximately 3.03 eV (vs normal hydrogen electrode (NHE)) based on the diffuse-reflectance spectrum (Figure S3b). The VB spectra for $TiO_2$ and $Ag_2S$ (Figure S3c,d) confirm their positions as 2.64 and 0.17 eV, respectively. It is worth noting that the VB of $Ag_2S$ equal to 0.17 eV in $TiO_2$−Ag−$Ag_2S$ composites is much lower than the known value of 0.92 eV for pure $Ag_2S$, which is favorable proof of an increase in the band gap of $Ag_2S$ in the system.[27] As a result, the two semiconductors, which used to have parallel band gaps, now appear to be interlaced, as shown in Scheme 2. However, the

**Scheme 2. Energy Band Diagram and Charge Separation Path for $TiO_2$−$Ag_2S$ and $TiO_2$−Ag−$Ag_2S$**

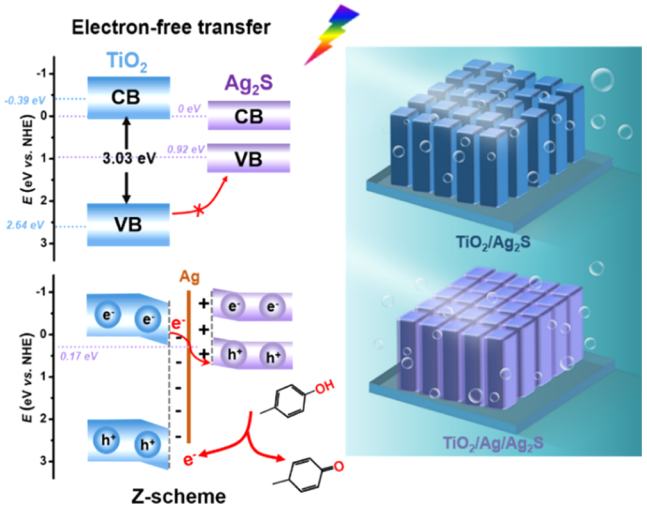


VB energy of $TiO_2$ is lower than the oxidation potential of hydroxyl radicals ($^{\bullet}OH$) at 2.7 eV (vs NHE), so it is not practical to confirm the Z-type heterojunction via EPR. The results confirm this conjecture that no significant increase in $^{\bullet}OH$ species is observed under prolonged Xe lamp irradiation compared to the dark treatment with dimethylpyridine *N*-oxide (DMPO) as a capturer (Figure S4).[28]

ISI-XPS was employed to further investigate the charge dynamics and heterojunction types.[29] As shown in Figure 3a, two peaks are found in the off-light state at 458.8 and 464.6 eV, which are attributed to Ti $2p_{3/2}$ and Ti $2p_{1/2}$, respectively. With Xe lamp irradiation, an evident positive shift of approximately 0.2 eV occurs in the Ti 2p binding energy. The shift of the characteristic peak toward the high-energy region confirms the decrease in the electron cloud density around Ti atoms.[30] As can be seen from Figure 3b, two characteristic peaks, Ag $3d_{5/2}$ and Ag $3d_{3/2}$, ascribed to monovalent $Ag^+$, are found at 367.1 and 373.2 eV, respectively, in the off-light state.[31] It is worth noting that the characteristic peaks of the elementary substance $Ag^0$ are decomposed in the Ag 3d spectrogram at binding energies of 368.1 and 374.0 eV. This is consistent with the XRD results and confirms that the

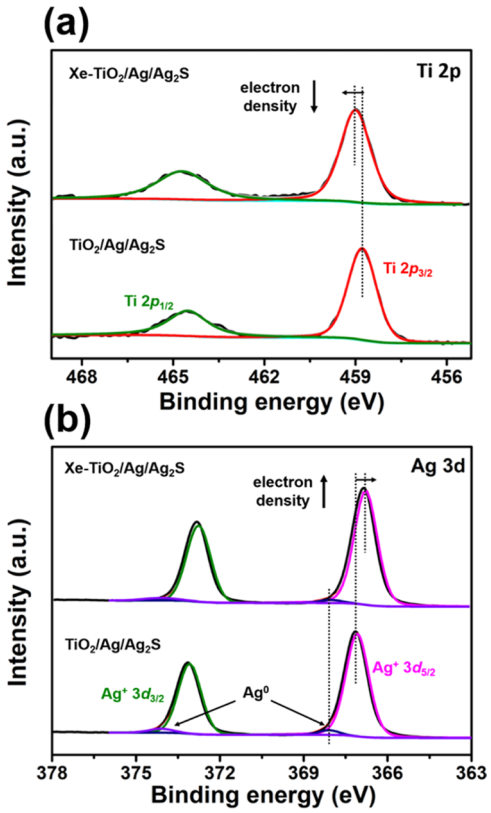


**Figure 3.** ISI-XPS spectra for (a) Ti 2p and (b) Ag 3d for $TiO_2$−Ag−$Ag_2S$ in the dark and under Xe lamp irradiation.

Ag layer is localized rather than completely sulfidated. The $Ag^+$ 3d binding energy shows a negative shift at approximately −0.3 eV with Xe lamp irradiation. The shift of the characteristic peak to the lower-energy region can only be explained as electron injection from the $TiO_2$ CB into the $Ag_2S$ VB (Scheme 2), leading to the aggregation of electrons around the Ag atom and an increase in the electron cloud density. Photocurrent density tests are commonly used to evaluate the generation and separation efficiency of $e^-/h^+$ pairs in materials. In Figure S5, $TiO_2$−Ag−$Ag_2S$ exhibits a higher photocurrent density than pure $TiO_2$ under Xe lamp interval irradiation within 140 s, which is indirect evidence for electron transport between $TiO_2$ and $Ag_2S$, and the test also confirms the excellent stability of the prepared sensing substrate. These results confirm that a Z-scheme ternary Ag-embedded $TiO_2$−$Ag_2S$ nanojunction was successfully obtained.

**Verification of the Rationality of CD44 Extraction.** Twelve percent poly(acrylamide) gel electrophoresis (PAGE) was employed to verify the rationality of CD44 extraction by an SRD method, and the results are shown in Figure 4. Hairpin DNA H1 and ssDNAs P1 and P2 show clear characteristic bands from Lanes 1 to 3. The bright band in Lane 4 reveals exhaustive base pairing between P1 and P2 and no byproducts or raw materials. With the release of P2, the SDR reaction is completed after the introduction of H1, several clear bands in Lane 5 can be attributed to P2, P1+P2, P1+H1 and P1+P2+H1, respectively. The results show that the as-proposed method for extracting CD44 is feasible.

**Electrochemical Impedance Spectroscopy (EIS) for Electrode Modification.** Electrochemical impedance spectroscopy (EIS) is commonly used to characterize stepwise modified electrodes. The inset of Figure 5a is Randles


https://doi.org/10.1021/acs.analchem.2c03046
Anal. Chem. 2022, 94, 11713−11720

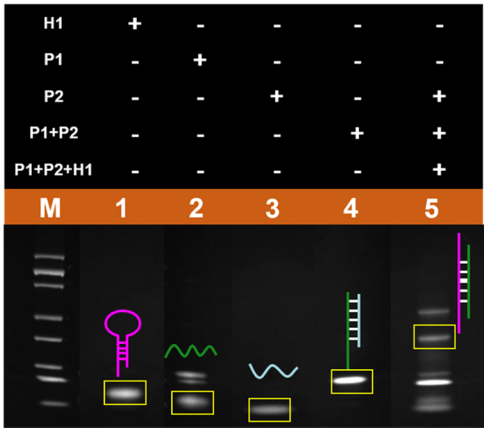


**Figure 4.** PAGE analysis for the SDR mechanism in the process of CD44 extraction (M: DNA maker; Lane 1: H1; Lane 2: P1; Lane 3: P2; Lane 4: P1 + P2; Lane 5: P1 + P2 + H1).

equivalent circuit containing Warburg impedance ($Z_w$), electron transfer impedance ($R_{et}$), solution impedance ($R_s$), and electrical double-layer capacitor ($C_{dl}$), and the corresponding simulation parameters are provided in Table S1. For pure FTO electrode, a small $R_{et}$ value is obtained around 24.59 Ω. $TiO_2$−Ag and $TiO_2$−Ag−$Ag_2S$ exhibit low $R_{et}$ values benefit from their excellent electrical conductivity compared with pure $TiO_2$. However, the sputtering of gold nanoparticles leads to a lower $R_{et}$ value of the $TiO_2$−Ag−$Ag_2S$/H1 layer. With the modification of signal label Y−P1−P2−HA, the impedance on the electrode surface increases clearly, which indicates successful biosensor fabrication.

**CD44 Analysis.** The as-fabricated sensing platform shows distinguishable PEC responses to CD44 produced on the surface of cells. The photocurrents are positively correlated with an increase in cell concentration ranging from 0 to 5 × $10^5$ cells/mL, and a dot plot similar to a logarithmic function is obtained, as shown in Figure 5b. When the cell concentrations are treated with a logarithm using 10 as the base number, we can obtain two linear relationships in the low- and high-concentration regions. The calibration curve for the low-concentration region is expressed as $P_1 = 0.560 \times \lg c - 0.122$ ($R_1^2 = 0.996$), with a detection range of 20−500 cells/mL. In the high-concentration regions (500 to 5 × $10^5$ cells/mL), the linear relationship between the PEC and logarithm of the concentration is expressed as $P_2 = 2.27 \times \lg c - 4.70$ ($R_2^2 = 0.997$). The limit of detection (LOD) of the sensor is calculated to be 37 cells/mL,[32] which is lower than that obtained in many representative reports (Table 1).

**Table 1. Comparison of Different Methods for CD44 Detection**

| methods | range (cells/mL) | LOD (cells/mL) | source |
|---|---|---|---|
| PEC | 5 × $10^1$−5 × $10^6$ | 50 | 33 |
| ECL | 5 × $10^2$−5 × $10^5$ | 150 | 34 |
| colorimetric | | 1000 | 35 |
| PEC | 1 × $10^2$−1 × $10^7$ | 100 | 36 |
| EC | 1 × $10^3$−1 × $10^6$ | 1000 | 24 |
| this work | 3.5 × $10^1$−1 × $10^5$ | 37 | |

**Property Evaluation.** The repeatability and stability of sensors depend on the microstructure of photoactive materials and the delicate design of the sensing units. To verify the above, one electrode was selected from each of the five batches and named electrodes 1−5. MDA-MB-231 cells (1 × $10^3$ cells/mL) were employed as targets under the same experimental conditions, and the results are shown in Figure 5c. The five tests show a relatively consistent photocurrent response with a relative standard deviation (RSD) of 4.43%. For stability, we selected two indices to evaluate the low- and high-

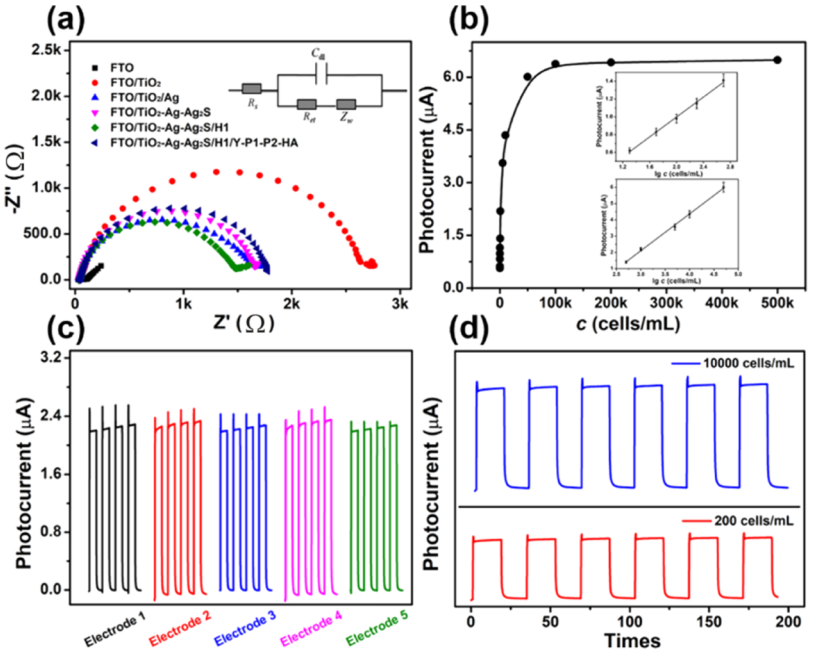


**Figure 5.** (a) EIS profiles of stepwise modified electrodes. (b) Positive correlation between photocurrent and cell numbers and the double linear calibration plot (inset) from 20 to 5 × $10^5$ cells/mL. Repeatability (c) and stability (d) tests for biosensors. Error bars: ±standard deviation (SD), $n$ = 11.



https://doi.org/10.1021/acs.analchem.2c03046
Anal. Chem. 2022, 94, 11713−11720

concentration regions. As shown in Figure 5d, the photocurrent at both concentrations is, without exception, extremely stable at 200 s of radiation. These results confirm the feasibility of using our proposed composite materials for cell analysis.

## CONCLUSIONS

In summary, the feasibility of well-ordered ternary Z-scheme $TiO_2$−Ag−$Ag_2S$ nanocomposite arrays for use as PEC sensing substrates and signal converters is demonstrated in this work. The $TiO_2$−Ag−$Ag_2S$ NAs prepared in three steps effectively improve the transfer path for photogenerated carriers while maintaining the original morphology of rod-like $TiO_2$, amplifying the photocurrent efficiency to reach the standard required for trace detection and providing highly accurate PEC stability. The formation of a "signal-on" biosensor with promising applications by conjugating MDA-MB-231 cells to extract CD44 on the surface benefits from the DNA chain reaction and host−guest recognition between HA and CD44, which enables the rapid and sensitive analysis of CD44 over a wide range of 37 to $5 \times 10^5$ cells/mL. This work showcases the capability of nanocomposite arrays to host and stabilize various biosensing units, which will be an essential and informative pathway for fabricating novel PEC converters for developing high-performance sensors for cell analysis.

## ASSOCIATED CONTENT

### Supporting Information

The Supporting Information is available free of charge at https://pubs.acs.org/doi/10.1021/acs.analchem.2c03046.

X-ray diffraction patterns; elemental mapping spectra; UV−vis absorption; band gap diagram; valence band spectra; electron paramagnetic resonance spectra; photocurrent density test; exploration of optimal pH; EIS simulation parameters; and limit of detection (PDF)

## AUTHOR INFORMATION


### Corresponding Authors

**Yuyang Li** − *Key Laboratory of Interfacial Reaction and Sensing Analysis in Universities of Shandong, School of Chemistry and Chemical Engineering, University of Jinan, Jinan 250022, China;* orcid.org/0000-0002-1399-9381; Email: chm_liyy@ujn.edu.cn

**Qin Wei** − *Key Laboratory of Interfacial Reaction and Sensing Analysis in Universities of Shandong, School of Chemistry and Chemical Engineering, University of Jinan, Jinan 250022, China;* orcid.org/0000-0002-3034-8046; Email: sdjndxwq@163.com

### Authors

**Yue Jia** − *Key Laboratory of Interfacial Reaction and Sensing Analysis in Universities of Shandong, School of Chemistry and Chemical Engineering, University of Jinan, Jinan 250022, China*

**Rui Xu** − *Key Laboratory of Interfacial Reaction and Sensing Analysis in Universities of Shandong, School of Chemistry and Chemical Engineering, University of Jinan, Jinan 250022, China*

**Kun Xu** − *Key Laboratory of Interfacial Reaction and Sensing Analysis in Universities of Shandong, School of Chemistry and Chemical Engineering, University of Jinan, Jinan 250022, China*

**Shoufeng Wang** − *Key Laboratory of Interfacial Reaction and Sensing Analysis in Universities of Shandong, School of Chemistry and Chemical Engineering, University of Jinan, Jinan 250022, China;* orcid.org/0000-0002-5575-5772

**Xiang Ren** − *Key Laboratory of Interfacial Reaction and Sensing Analysis in Universities of Shandong, School of Chemistry and Chemical Engineering, University of Jinan, Jinan 250022, China;* orcid.org/0000-0002-4321-4282

**Nuo Zhang** − *Key Laboratory of Interfacial Reaction and Sensing Analysis in Universities of Shandong, School of Chemistry and Chemical Engineering, University of Jinan, Jinan 250022, China*

**Dan Wu** − *Key Laboratory of Interfacial Reaction and Sensing Analysis in Universities of Shandong, School of Chemistry and Chemical Engineering, University of Jinan, Jinan 250022, China;* orcid.org/0000-0002-8732-5988

**Hongmin Ma** − *Key Laboratory of Interfacial Reaction and Sensing Analysis in Universities of Shandong, School of Chemistry and Chemical Engineering, University of Jinan, Jinan 250022, China;* orcid.org/0000-0002-7061-8944

Complete contact information is available at: https://pubs.acs.org/10.1021/acs.analchem.2c03046


### Author Contributions

†Y.J. and R.X. contributed equally to this paper.

### Notes

The authors declare no competing financial interest.

## ACKNOWLEDGMENTS

This work was supported by the National Natural Science Foundation of China (no. 51904114), the Special Foundation for Taishan Scholar Professorship of Shandong Province (nos. ts20130937, ts201712052), and the Shandong Provincial Natural Science Foundation (no. ZR2020QB097). The authors thank Yankai Li from Shiyanjia Lab (www.shiyanjia.com) for the ISI-XPS analysis.

## REFERENCES


(1) Zhao, W.-W.; Xu, J.-J.; Chen, H.-Y. *Chem. Rev.* **2014**, *114*, 7421−7441.

(2) Zhao, W.-W.; Xu, J.-J.; Chen, H.-Y. *Chem. Soc. Rev.* **2015**, *44*, 729−741.

(3) Zhou, Q.; Tang, D. *TrAC Trends Anal. Chem.* **2020**, *124*, No. 115814.

(4) Yang, L.; Xue, J.; Jia, Y.; Zhang, Y.; Wu, D.; Ma, H.; Wei, Q.; Ju, H. *Biosens. Bioelectron.* **2019**, *142*, No. 111562.

(5) Wang, L.; Zhao, J.; Liu, H.; Huang, J. *J. Taiwan Inst. Chem. Eng.* **2018**, *93*, 590−602.

(6) Chen, X.; Selloni, A. *Chem. Rev.* **2014**, *114*, 9281−9282.

(7) Li, W.; Elzatahry, A.; Aldhayan, D.; Zhao, D. *Chem. Soc. Rev.* **2018**, *47*, 8203−8237.

(8) Zhang, Y.; Liu, J.-X.; Qian, K.; Jia, A.; Li, D.; Shi, L.; Hu, J.; Zhu, J.; Huang, W. *Angew. Chem., Int. Ed.* **2021**, *60*, 12074−12081.

(9) Xie, J.; Xie, H.; Su, B.-L.; Cheng, Y.-b.; Du, X.; Zeng, H.; Wang, M.; Wang, W.; Wang, H.; Fu, Z. *Angew. Chem., Int. Ed.* **2016**, *55*, 3031−3035.

(10) Gao, C.; Wei, T.; Zhang, Y.; Song, X.; Huan, Y.; Liu, H.; Zhao, M.; Yu, J.; Chen, X. *Adv. Mater.* **2019**, *31*, No. 1806596.

(11) Wang, J.; Shen, Y.; Liu, S.; Zhang, Y. *Appl. Catal., B* **2020**, *270*, No. 118885.

(12) Zhou, Y.; Wang, H.; Zhuo, Y.; Chai, Y.; Yuan, R. *Anal. Chem.* **2017**, *89*, 3732−3738.

(13) Tada, H.; Mitsui, T.; Kiyonaga, T.; Akita, T.; Tanaka, K. *Nat. Mater.* **2006**, *5*, 782−786.

(14) Yu, H.; Liu, W.; Wang, X.; Wang, F. *Appl. Catal., B* **2018**, *225*, 415−423.
(15) Gao, H.; Zhang, P.; Hu, J.; Pan, J.; Fan, J.; Shao, G. *Appl. Surf. Sci.* **2017**, *391*, 211−217.
(16) Guo, Y.; Xiao, L.; Zhang, M.; Li, Q.; Yang, J. *Appl. Surf. Sci.* **2018**, *440*, 432−439.
(17) Li, Y.; Li, L.; Gong, Y.; Bai, S.; Ju, H.; Wang, C.; Xu, Q.; Zhu, J.; Jiang, J.; Xiong, Y. *Nano Res.* **2015**, *8*, 3621−3629.
(18) Ong, W. J.; Tan, L. L.; Ng, Y. H.; Yong, S. T.; Chai, S. P. *Chem. Rev.* **2016**, *116*, 7159−7329.
(19) Xing, X.; Zhu, H.; Zhang, M.; Hou, L.; Li, Q.; Yang, J. *Catal. Sci. Technol.* **2018**, *8*, 3629−3637.
(20) Knies, M.; Kaiser, M.; Isaeva, A.; Müller, U.; Doert, T.; Ruck, M. *Chem. - Eur. J.* **2018**, *24*, 1.
(21) Zheng, X.; Yang, L.; Li, Y.; Yang, L.; Luo, S. *Electrochim. Acta* **2019**, *298*, 663−669.
(22) Li, Q.; Xia, Y.; Yang, C.; Lv, K.; Lei, M.; Li, M. *Chem. Eng. J.* **2018**, *349*, 287−296.
(23) Kwon, M. Y.; Wang, C.; Galarraga, J. H.; Puré, E.; Han, L.; Burdick, J. A. *Biomaterials* **2019**, *222*, No. 119451.
(24) Zhang, R.; Rejeeth, C.; Xu, W.; Zhu, C.; Liu, X.; Wan, J.; Jiang, M.; Qian, K. *Anal. Chem.* **2019**, *91*, 7078−7085.
(25) Jia, Y.; Zhang, N.; Du, Y.; Ren, X.; Ma, H.; Wu, D.; Fan, D.; Wei, Q.; Ju, H. *Biosens. Bioelectron.* **2022**, *210*, No. 114291.
(26) Fang, C.; Lee, Y. H.; Shao, L.; Jiang, R.; Wang, J.; Xu, Q.-H. *ACS Nano* **2013**, *7*, 9354−9365.
(27) Feng, J.; Qian, Y.; Cheng, Q.; Ma, Y.; Wu, D.; Ma, H.; Ren, X.; Wang, X.; Wei, Q. *Biosens. Bioelectron.* **2020**, *168*, No. 112503.
(28) Xing, H.; Peng, C.; Xue, Y.; Fan, Y.; Li, J.; Wang, E. *Anal. Chem.* **2020**, *92*, 10108−10113.
(29) Liu, X.; Dong, G.; Li, S.; Lu, G.; Bi, Y. *J. Am. Chem. Soc.* **2016**, *138*, 2917−2920.
(30) Low, J.; Dai, B.; Tong, T.; Jiang, C.; Yu, J. *Adv. Mater.* **2019**, *31*, No. 1802981.
(31) Ye, L.; Liu, J.; Gong, C.; Tian, L.; Peng, T.; Zan, L. *ACS Catal.* **2012**, *2*, 1677−1683.
(32) Ren, K.; Wu, J.; Yan, F.; Zhang, Y.; Ju, H. *Biosens. Bioelectron.* **2015**, *66*, 345−349.
(33) Gao, N.; Fan, B.; Li, L.; Sun, X.; Wang, X.; Ma, H.; Wei, Q.; Ju, H. *ACS Appl. Bio Mater.* **2021**, *4*, 4479−4485.
(34) Zhang, L.; Wang, Y.; Tian, Q.; Liu, Y.; Li, J. *Biosens. Bioelectron.* **2017**, *89*, 1013−1019.
(35) Tao, Y.; Lin, Y.; Huang, Z.; Ren, J.; Qu, X. *Adv. Mater.* **2013**, *25*, 2594−2599.
(36) Li, R.; Tu, W.; Wang, H.; Dai, Z. *Anal. Chem.* **2018**, *90*, 9403−9409.





https://doi.org/10.1021/acs.analchem.2c03046
*Anal. Chem.* 2022, 94, 11713−11720